Supplementary Information (SI) for Journal of Materials Chemistry A.

Supporting Information

Mitigating Trap States in Halide Perovskite Solar Cells Through the Synergy of Coordination, Hydrogen and Halogen Types of Bonding

Yuling Zhuo,[a, b] *Tongjun Zheng,*[a, b] *Shuguang Cao,*[a, b] *Shizi Luo,*[a, b] *Zhuoneng Bi,**[a, b] *Yupeng Zheng,*[b] *Biniyam Zemene Taye,*[a, b] *Xiaoli Chen,*[b] *Lavrenty G. Gutsev,**[c, g] *Victoria V. Ozerova,*[c] *Nikita A. Emelianov,*[c] *Sergey G. Vasil'ev,*[c] *Alexander F. Shestakov,*[c] *Hao Li,*[d] *Chao Wang,*[e] *Yanping Mo,**[e] *Gennady L. Gutsev,*[h] *Balu R. Ramachandran,*[g] *Ning Li,*[d] *Eric N Maluta,*[i] *Sergey M. Aldoshin,*[c] *Pavel A. Troshin,**[c, f] *and Xueqing Xu**[a, b]

[a]School of Energy Science and Engineering, University of Science and Technology of China, Hefei, 230026, P.R. China
[b]Guangzhou Institute of Energy Conversion, Chinese Academy of Sciences, CAS Key Laboratory of Renewable Energy, Guangdong Provincial Key Laboratory of Renewable Energy, Guangzhou 510640, P. R. China
[c]Federal Research Center for Problems of Chemical Physics and Medicinal Chemistry of RAS, Academician Semenov ave. 1, Chernogolovka, 142432, Russia
[d]Institute of Polymer Optoelectronic Materials and Devices State Key Laboratory of Luminescent Materials and Devices, South China University of Technology, Guangzhou 510640, P. R. China
[e]Foshan Xianhu Laboratory of the Advanced Energy Science and Technology Guangdong Laboratory, Foshan, 528216, PR China
[f]Zhengzhou Research Institute of HIT, 26 Longyuan East 7th, Jinshui District, Zhengzhou, Henan Province 450000, PR China
[g]Institute for Micromanufacturing, Louisiana Tech University, Ruston, LA 71272, United States
[h]Department of Physics, Florida A&M 711 University, Tallahassee, Florida 32307, United States
[i]Green Technology Confucius Institute, University of Venda, Thohoyandou, 0950, South Africa

Experimental sections

Materials

N,N-dimethylformamide (DMF, 99.8%), dimethylsulfoxide (DMSO, >99.5%), ethyl acetate (EA, anhydrous, 99.8%) and chlorobenzene (CB, 99.8%) were purchased from Sigma-Aldrich. Isopropanol (IPA, anhydrous, 99.8%) was purchased from Acros. Ethanol (GR, Water≤0.2%) was purchased from Aladdin. Lead(II) iodide (PbI_2, 99.99%) was purchased from Advanced Election Technology Co., Ltd. Lead(II) bromine ($PbBr_2$), methylammonium chloride (MACl), formamidinium iodide (FAI), methylammonium bromide (MABr), Cesium iodide (CsI), [6,6]-phenyl-C_{61}-butyric acid methyl ester (PCBM) and bathocuproine (BCP) were purchased from Xi'an Yuri Solar Co., Ltd.[4-(3,6-Dimethyl-9H-carbazol-9-yl)butyl]phosphonic acid (Me-4PACz) was purchased from TCI. 4-bromo-2,6-difluorobenzonitrile (BrFBN), 4-bromo-2,6-difluoroaniline (BrFBA) and 4-bromo-2,6-difluorophenol (BrFBP) were purchased from Macklin. Nickel oxide particle (NiO_x) was purchased from Suzhou Kejingte Intelligent Technology Co., Ltd.

Preparation of pristine and molecule-doped perovskite precursor solution

7.7 mg MABr, 10.2 mg MACl, 21.0 mg CsI, 25.4 mg $PbBr_2$, 226.7 mg FAI and 661.3 mg PbI_2 were dissolved in 1 mL DMF and DMSO solution (volume ratio 4: 1) and stirred for 2 h without heat to prepare undoped precursor solution. For doped solution, another 2~4 mg passivation reagent (BrFBN, BrFBP or BrFBA) was added in the preceding solution.

Device fabrication

The glass/ITO substrates (purchased from Advanced Election Technology Co., Ltd) were ultrasonically cleaned with detergent (5% in deionized water), deionized water, ethanol, and isopropanol each for 20 min, respectively. Then, the glass/ITO substrates were dried at 80 °C in an oven, and then were treated with UV-Ozone (UVO) for 15 min. NiO_X nanoparticles were dispersed in deionized water at a concentration of 20 mg/mL to form NiO_X ink. The as-prepared NiO_X ink was spin-coated onto the ITO substrate at 3,000 rpm. for 30s, then annealing at 100 °C for 10 min in ambient air. and finally transferred into a N_2-filled glovebox immediately. 60 μL of Me-4PACz in ethanol (0.3 mg/mL) solution was spin-coated at 4000 rpm for 30 s inside the nitrogen-filled glovebox and annealed at 100 °C for 10 min. The as-prepared perovskite precursor solution was spin-coated onto the ITO/NiO_X/Me-4PACz substrate with speed of 1000 rpm for 5 s and 4000 rpm for 30 s. During the last 15 s of the spinning process, the liquid film was treated by drop-casting EA solvent (150 μL). The substrates were annealed on a hot plate at 100 °C for 50 min, and PEAI with concentration of 1.5 mg/mL in IPA and DMSO solution (volume ratio 200:1) was dynamically spin-coated on top (4000 rpm, 30 s) and annealed at 100 °C for 5 min. Then a layer of PCBM (20 mg/mL in chlorobenzene, 4000 rpm, 30 s) was coated and annealed at 100 °C for 5 min, followed by spin-coating BCP with concentration of 0.5 mg/mL in IPA on top (4000 rpm, 30 s). Finally, 80 nm thick of Ag was deposited on top by thermal evaporation.

Characterization

ESP calculations were performed calculated at B3LYP/6–31G (d, p) level with Grimme's D3BJ empirical dispersion correction by Gaussian 09. The dynamic light scattering (DLS) measurement was conducted by Zetasizer Nano ZS. The annealing process of perovskite films was observed with the help of OLYMPUS-MX63 optical microscope.

Nuclear magnetic resonance (NMR) spectra were collected using a Bruker 500MHz FT-NMR instrument spectrometer (Bruker, AVANCE III). Fourier transform infrared (FT-IR) spectrum were collected by Thermo Scientific Nicolet 6700. The top-view morphologies were examined by scanning electron microscopy (SEM, SU-70, Hitachi, Japan). The IR s-SNOM measurements were carried out using a neaSNOM microscope

(Neaspec, Haar, Germany) in PsHet mode with a Mid-IR laser MIRcat-2400 (Daylight Solutions, USA) installed inside the MBraun glove box (O_2, H_2O < 0.1 ppm).

The X-ray diffraction (XRD) patterns were acquired at room temperature on a Philips X'Pert PRO MPD X-ray diffractometer equipped with Cu-Kα radiation. X-ray photoelectron spectroscopy (XPS) measurements were done using Thermo Fisher Escalab 250Xi analyzer. Ultraviolet photoelectron spectra (UPS) were recorded using Kratos Axis Supra+, with the HeI (21.22 eV) emission line employed for excitation.

The steady-state photoluminescence (PL) and time-resolved PL (TRPL) spectra were recorded at room temperature using an Edinburgh fluorescence spectrometer (FLS980). UV-vis spectra of the perovskite films were obtained on a Lambda750 UV–vis–NIR spectrophotometer. The water contact angle was obtained using a contact angle measuring instrument (JD-901A).

For *J-V* measurements, the intensity of the light was 100 mW/cm^2 (simulated AM 1.5 G) provided by ABET Sun 3000 solar simulator and calibrated by a standard silicon reference cell. The *J-V* curves, space charge-limited current (SCLC) and electrochemical impedance spectroscopy (EIS) measurements for the solar cells were performed using Autolab TYPE II electrochemical work station. The external quantum efficiency (EQE) spectra of the solar cells were obtained using QTest Hifinity 5 (Crowntech, USA).

The operational stability of the PSCs was studied at maximum power point tracking (MPPT) using a 100 mW/cm^2 white LED lamp (Suzhou D&R Instrument Co., Ltd.) in an N_2-filled glove box.

Computational Methods

Molecular docking calculations were carried out using the GAUSSIAN 09 suite with the hybrid B3LYP functional. The 6-311G* basis set was employed for organic atoms, while the Lanl2Dz basis set was used for Pb and I. To account for dispersion interactions, the D3 dispersion correction was included.[1] For the docking study, a monolayer of PbI_2 (ML-PbI_2) was modeled as a 5×5×1 cluster ($Pb_{25}I_{50}$). This study specifically examined the passivants 4-bromo-2,6-difluorobenzonitrile (BrFBN), 4-bromo-2,6-difluoroaniline (BrFBA), and 4-bromo-2,6-difluorophenol (BrFBP), with a particular focus on BrFBN. Docking calculations involved placing BrFBN at various adsorption sites on the ML-PbI_2 cluster, including I-rich, Pb-moderate, and Pb-rich regions. To preserve structural integrity, only the geometry of BrFBN was allowed to relax during optimization, while the PbI_2 cluster was kept frozen. This constraint prevented the cluster from forming I_3 chains or Pb(0) species at its terminations, which could otherwise compromise the simulation. The adsorption energy (E_{ads}) of BrFBN on the PbI_2 cluster was calculated using the equation:

$$E_{ads}(D^q) = E_{PbI_2/pass}(D^q) - E_{PbI_2}(D^q) - E_{pass} \#(Equation\ S1)$$

Here, D^q denotes whether the species is pristine or defective, $E_{PbI_2/pass}(D^q)$ is the total energy of the PbI_2 cluster with BrFBN adsorbed, $E_{PbI_2}(D^q)$ is the energy of the bare PbI_2 cluster, and E_{pass} is the energy of the isolated BrFBN molecule. Solvent continuum Reaction Field (SCRF) were included with parameters corresponding to H_2O.[2]

For adsorption on perovskite surfaces, we used the Vienna Ab initio Simulation Package (VASP).[3] Momentum space sampling was initially performed at the Gamma-point and later refined to a 2×2×1 grid. The PBE functional, combined with D3 dispersion corrections, was employed.[4, 5] Projector augmented-wave (PAW) pseudopotentials were utilized with a plane-wave energy cutoff of 520 eV, which was confirmed as sufficient, as increasing the cutoff to 650 eV yielded negligible energy changes. Non-spherical contributions to the gradient within PAW spheres were also included, as these improve the accuracy of observables for perovskite oxides.[6-8] Adsorption energy calculations on the $FAPbI_3$ surface used the same methodology as for PbI_2, substituting PbI_2 with $FAPbI_3$ in the equation. The α-$FAPbI_3$ (100) surface served as the base model for constructing supercells, with the (100) direction defined as the “z-axis.” This surface type was chosen since it appears to grow preferentially according to our experimental data discussed in the main text. Supercells with dimensions of 3×3×5 were used, providing a balance between computational cost and accuracy. A vacuum layer of 20 Å was included above the $FAPbI_3$ surface to minimize interactions between periodic images. Calculations allowed full relaxation of atomic positions and lattice constants, constrained only by a fixed cell volume (ISIF = 4 in VASP). This study highlights the adsorption behavior of BrFBN, which exhibits strong interaction with both PbI_2 clusters and $FAPbI_3$ surfaces, suggesting its potential as a robust passivant for these materials.

Result and Discussion

Note 1: TRPL[9]

The TRPL decay curves are fitted by the bi-exponential function equation S2 and the fitted data are summarized in Table S1

$$I(t) = I_0 + A_1\exp\left(-\frac{t}{\tau_1}\right) + A_2\exp\left(-\frac{t}{\tau_2}\right) \qquad \text{(Equation S2)}$$

where, τ_1 is the fast decay process related to bimolecular recombination, and τ_2 is the slow decay process associated with trap-assisted recombination. I_0 is a constant for the baseline offset. A_1 and A_2 are constants.

τ_{ave} can be calculated by the equation S3

$$\tau_{ave} = \frac{A_1 \times \tau_1^2 + A_2 \times \tau_2^2}{A_1 \times \tau_1 + A_2 \times \tau_2} \qquad \text{(Equation S3)}$$

Note 2: The relationship between light intensity and V_{OC}[10]

$$V_{OC} \propto n\frac{kT}{q}\ln I \qquad \text{(Equation S4)}$$

the deviation of the slope illustrates that there is trap-assisted recombination in PSCs, where n is the ideality factor, k is the Boltzmann constant, T is the absolute temperature, and q is the elementary charge.

Note 3: SCLC[11]

The trap density (N_t) of perovskite films is calculated by the equation S5

$$N_t = \frac{2V_{TFL}\varepsilon_0\varepsilon_r}{eL^2} \qquad \text{(Equation S5)}$$

where V_{TFL} is the trap-filled limit voltage, L is the thickness of perovskite, ε is the relative permittivity of the perovskite (46.9), and ε_0 is the vacuum permittivity.

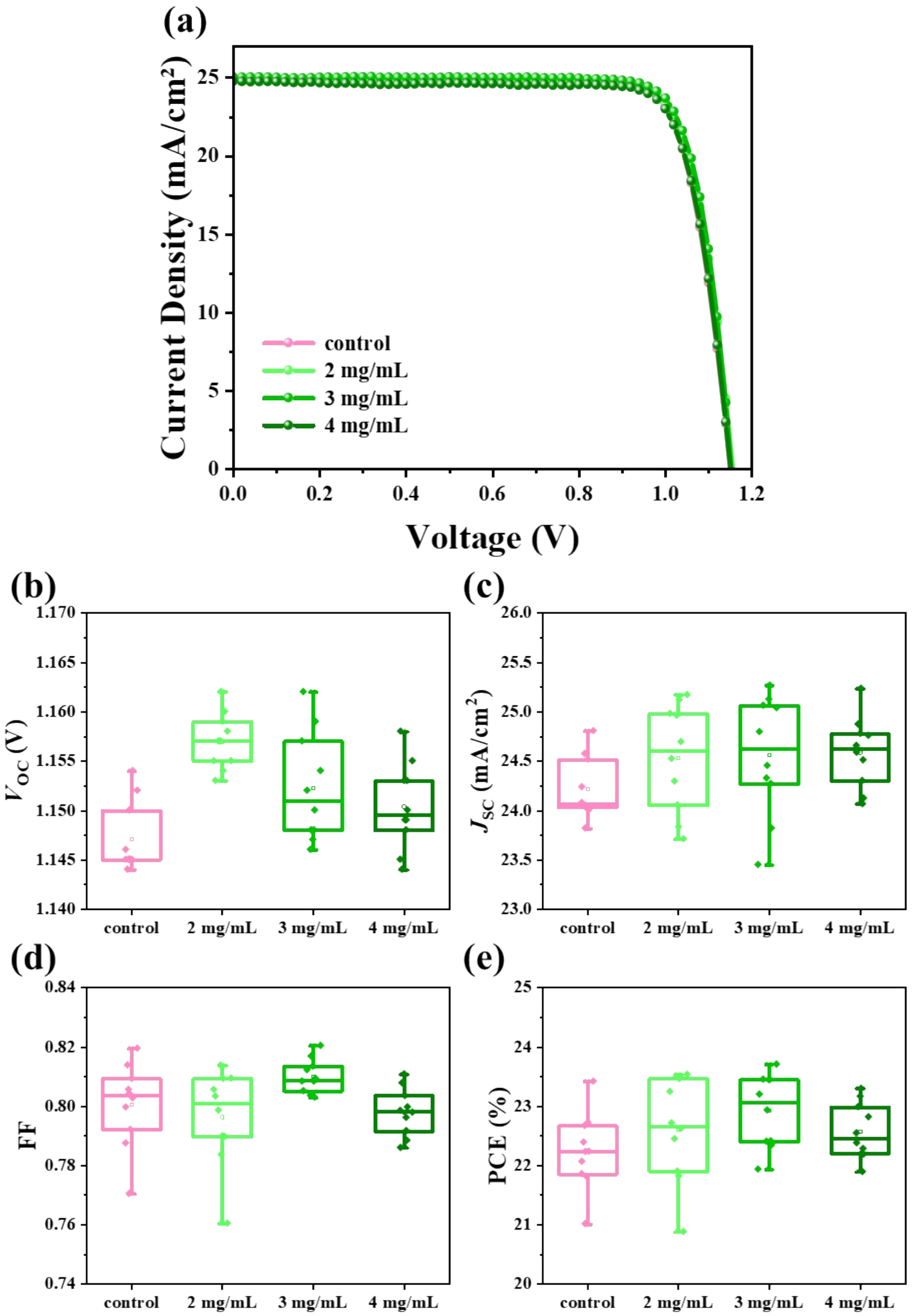

Figure S1. (a) *J*-*V* characteristics of champion device processed with various concentrations of BrFBA additive in the reverse scan. Histogram of (b) V_{OC} (c) J_{SC} (d) FF and (e) PCE for 10 devices.

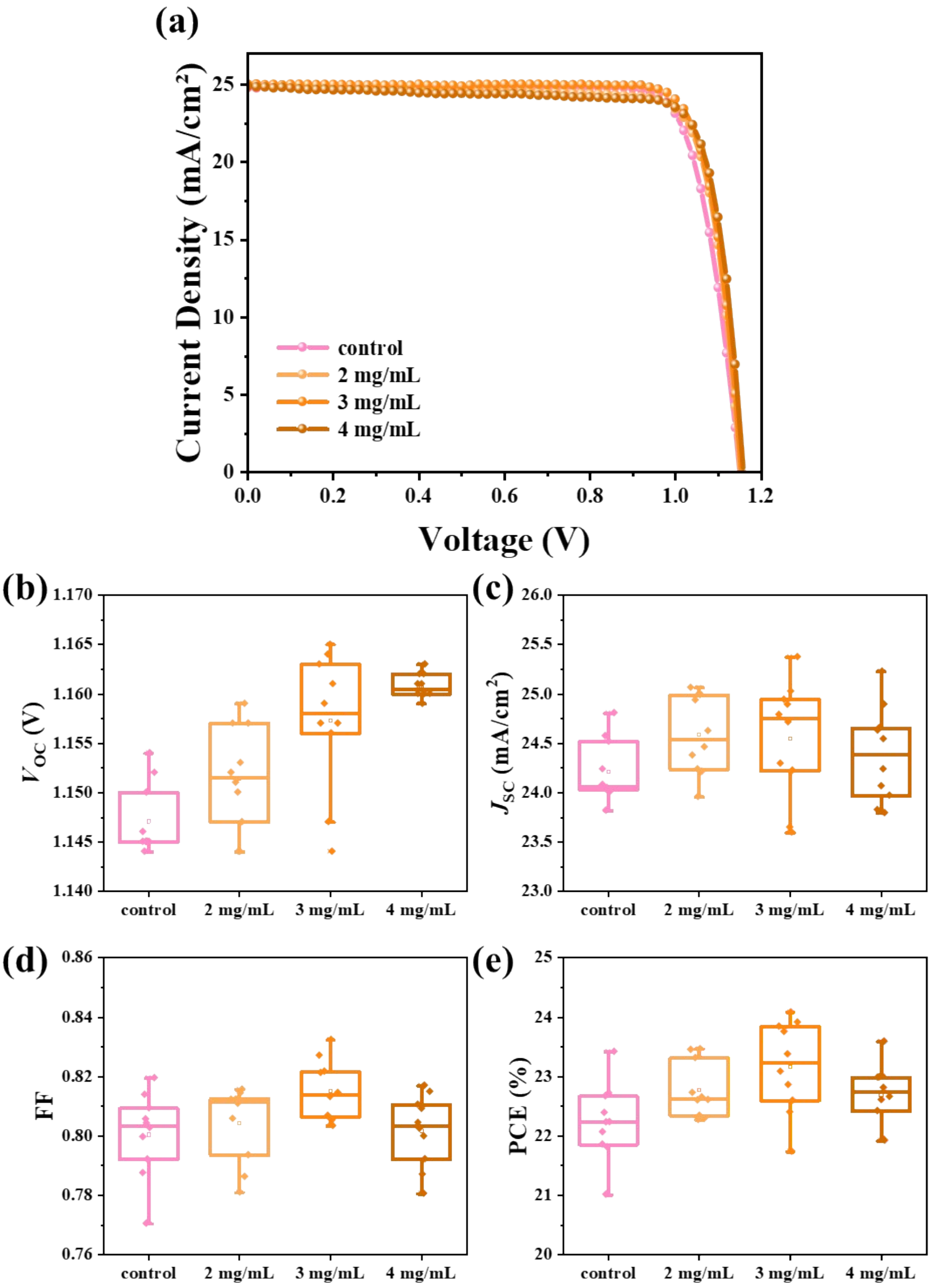

Figure S2. (a) *J*-*V* characteristics of champion device processed with various concentrations of BrFBP additive in the reverse scan. Histogram of (b) V_{OC} (c) J_{SC} (d) FF and (e) PCE for 10 devices.

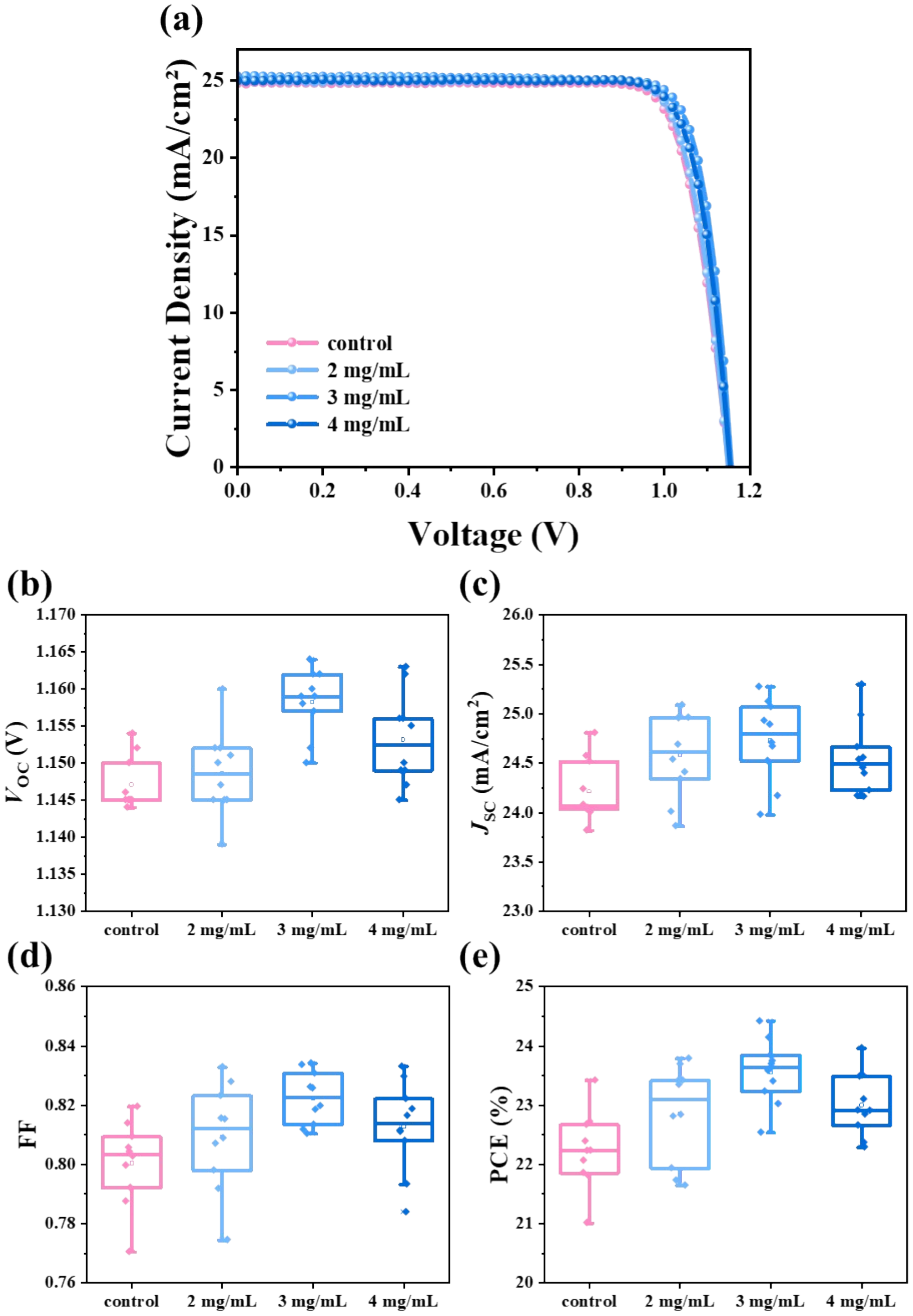

Figure S3. (a) *J*-*V* characteristics of champion device processed with various concentrations of BrFBN additive in the reverse scan. Histogram of (b) V_{OC} (c) J_{SC} (d) FF and (e) PCE for 10 devices.

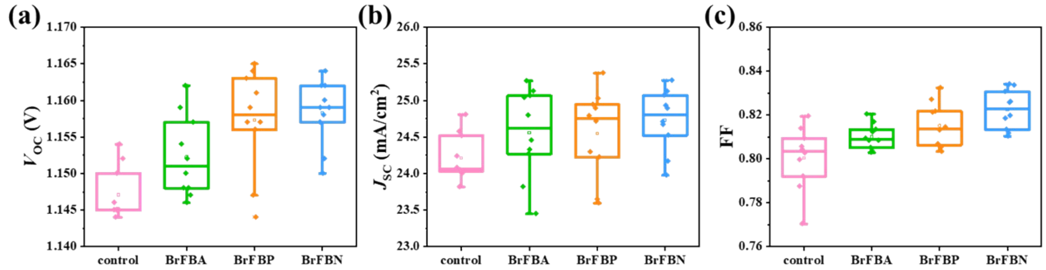

Figure S4. Histogram of (a) V_{OC} (b) J_{SC} and (c) FF for 10 devices (PSCs with the best additive concentration).

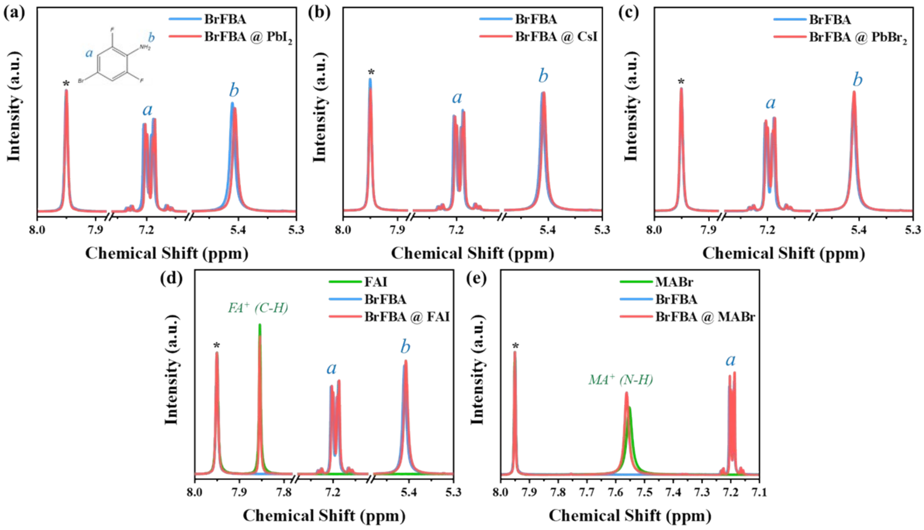

Figure S5. ^{1}H NMR spectra of BrFBA mixed with different perovskite precursor components. All samples were dissolved in DMSO-d6 solvent.

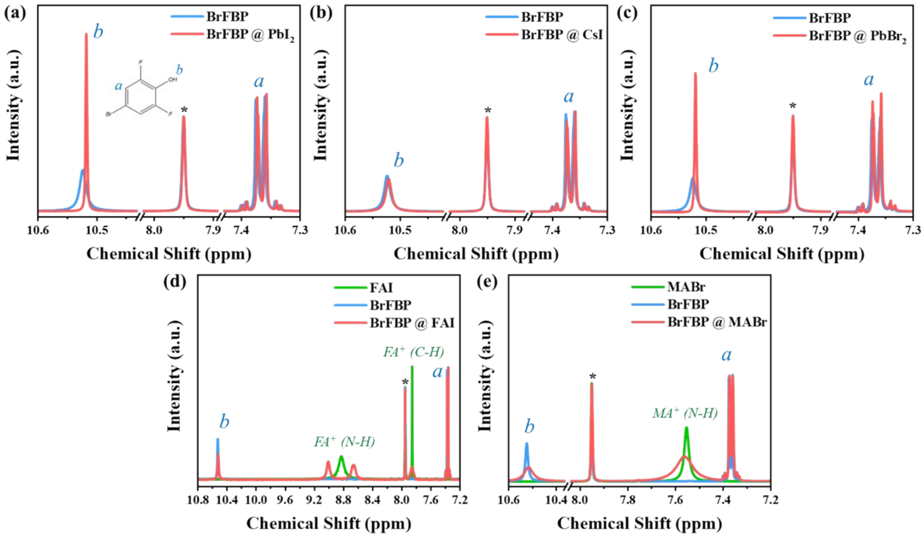

Figure S6. ^{1}H NMR spectra of BrFBP mixed with different perovskite precursor components. All samples were dissolved in DMSO-d6 solvent.

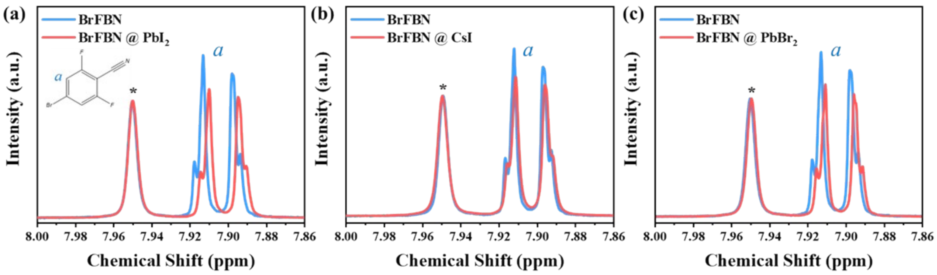

Figure S7. ^{1}H NMR spectra of BrFBN mixed with different perovskite precursor components. All samples were dissolved in DMSO-d6 solvent.

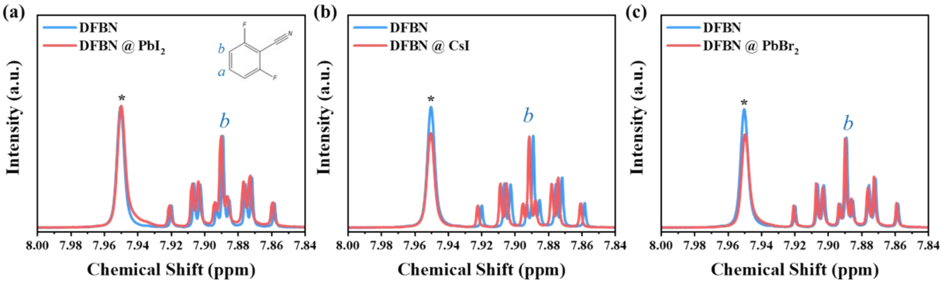

Figure S8. ^{1}H NMR spectra of DFBN mixed with different perovskite precursor components. All samples were dissolved in DMSO-d6 solvent.

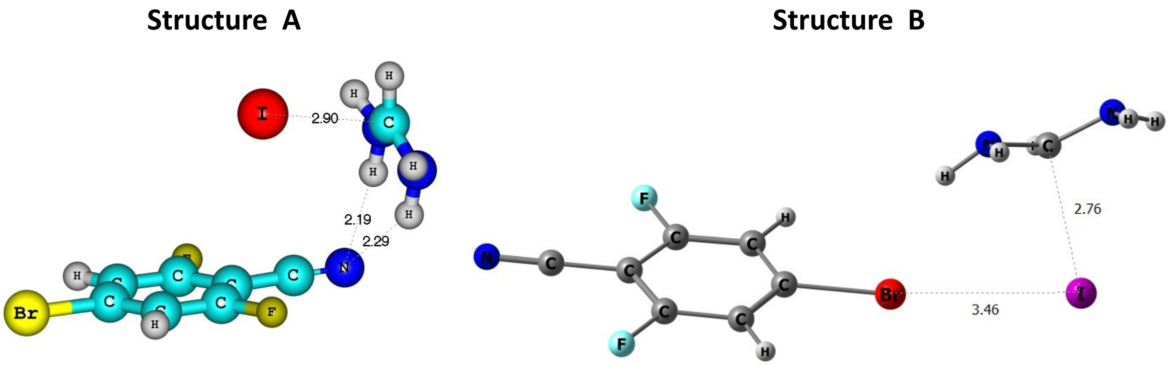

Figure S9. DFT computed geometries of two complexes of BrFBN with FAI: hydrogen-bonded structure A and structure B featuring Br···I$^-$ halogen bonding.

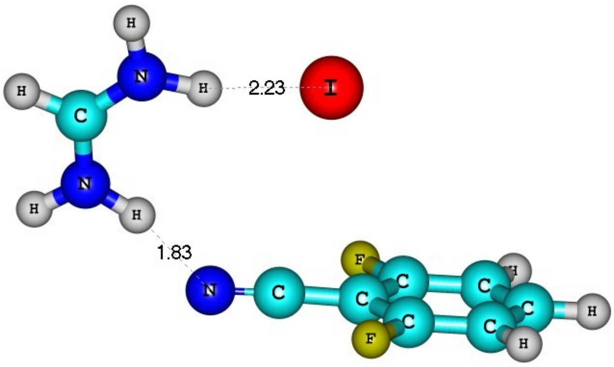

Figure S10. DFT computed geometry of the complex of DFBN with FAI featuring hydrogen-bonding of FA$^+$ cation with the nitrile group of DFBN and I$^-$ anion.

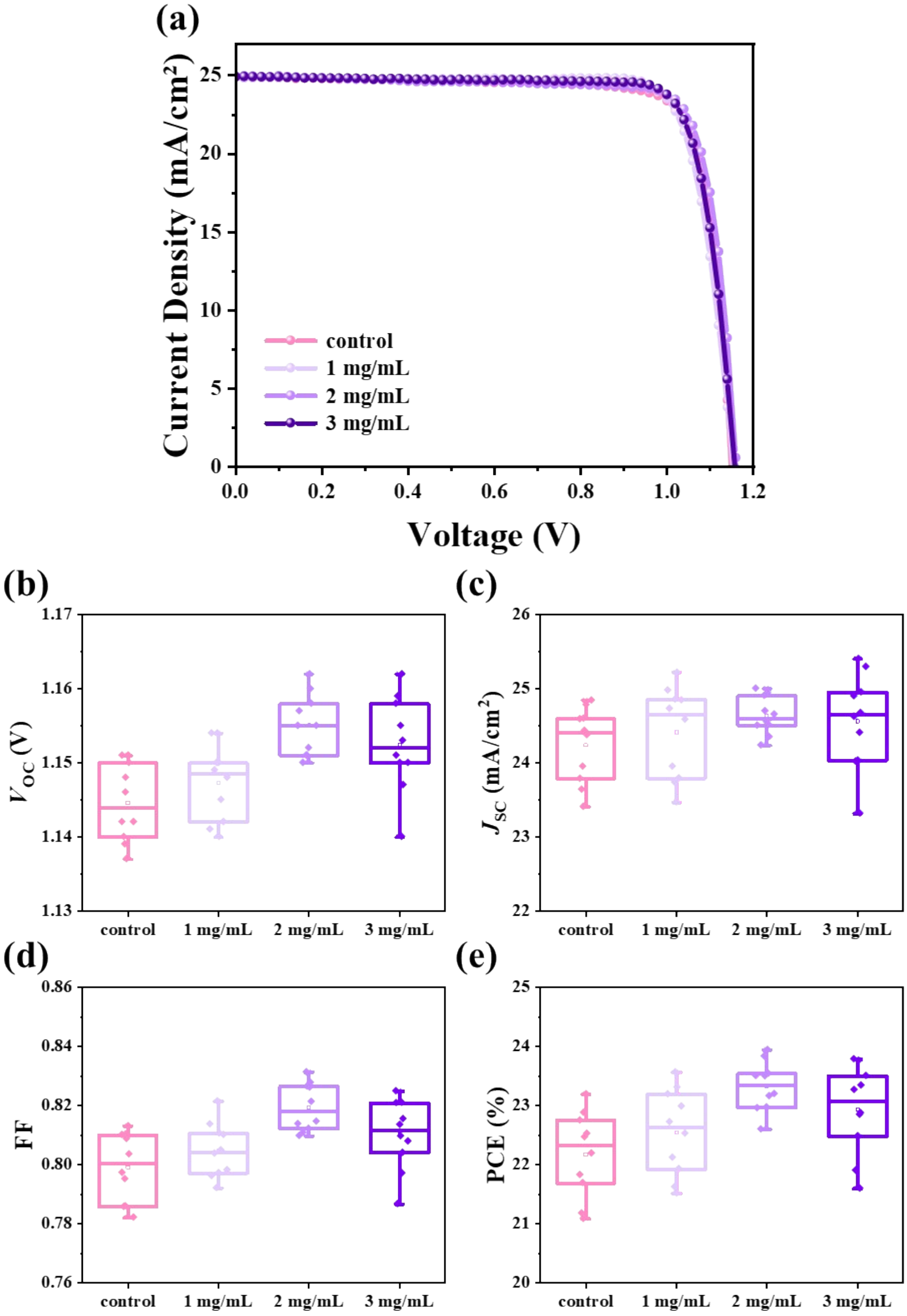

Figure S11. (a) *J*-*V* characteristics of champion device processed with various concentrations of DFBN additive in the reverse scan. Histogram of (b) V_{OC} (c) J_{SC} (d) FF and (e) PCE for 10 devices.

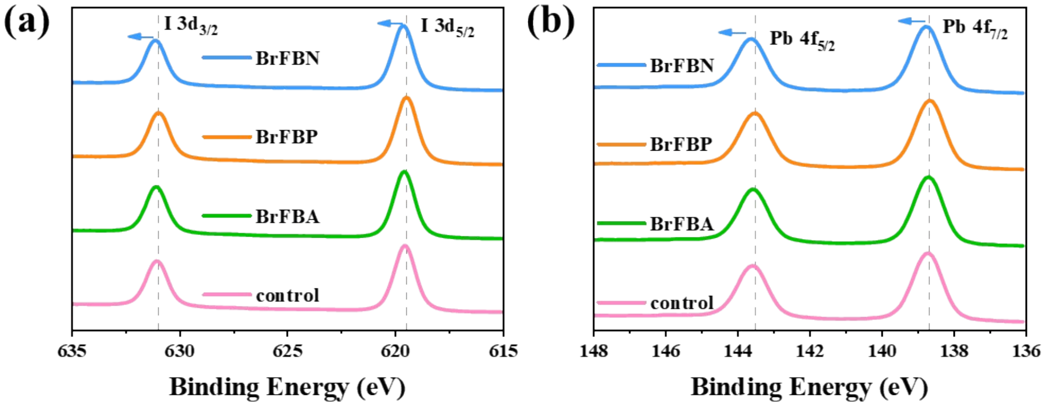

Figure S12. X-ray photoelectron spectra of different treatment perovskite films deposited on glass/ITO/HTL substructure corresponding to core levels of (a) I 3*d* and (b) Pb 4*f*.

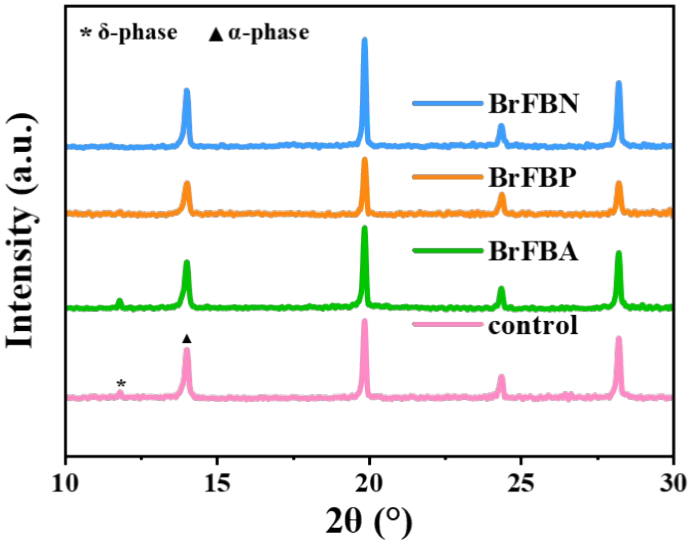

Figure S13. XRD patterns of various perovskite films without annealing.

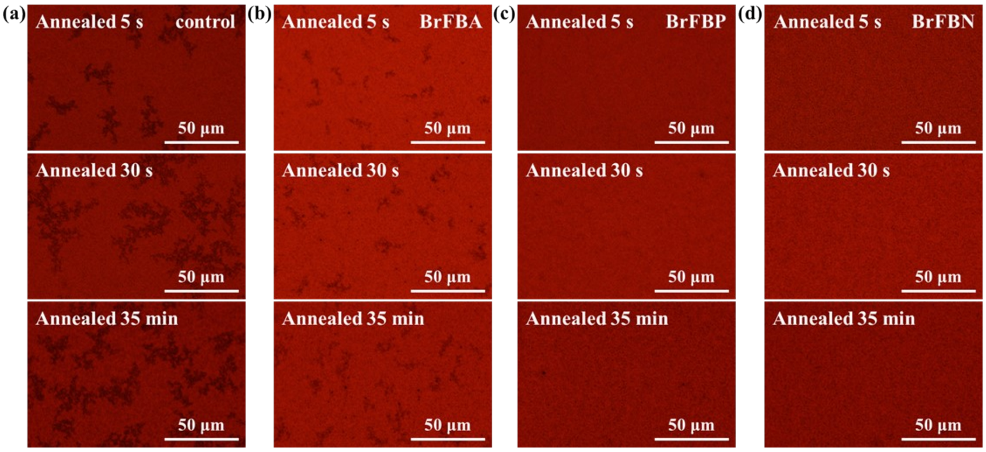

Figure S14. Optical microscope images of different treatment perovskite films after annealing for 5 s, 30 s and 35 min at 100 °C.

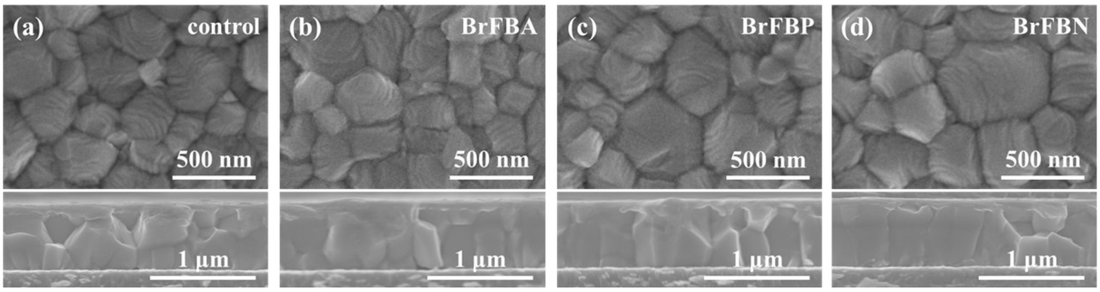

Figure S15. SEM images of different treatment perovskite films. Top row shows the top-view, and Bottom row shows the cross-view.

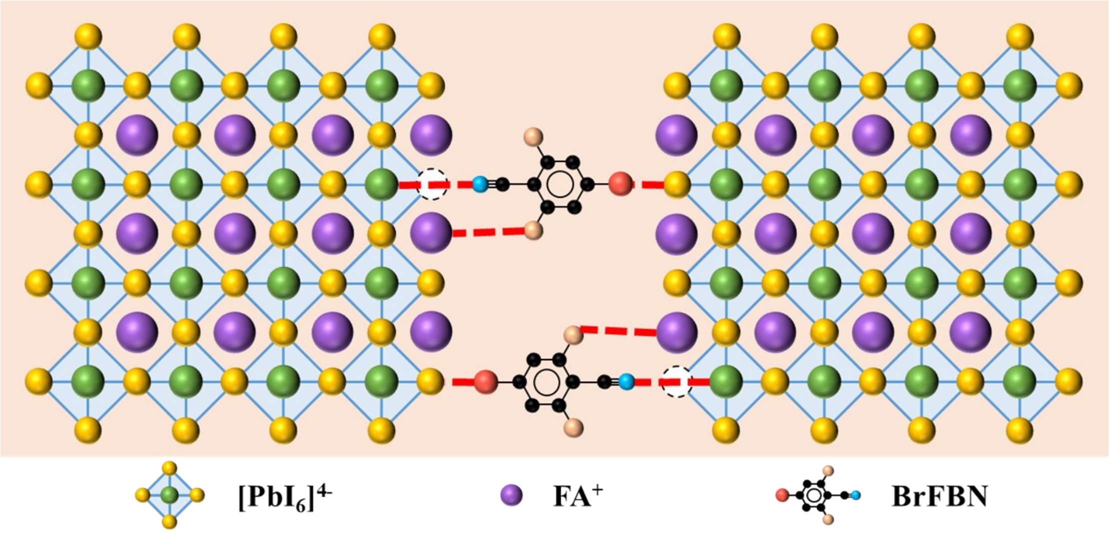

Figure S16. Schematic diagram of the interaction between BrFBN and perovskite crystals.

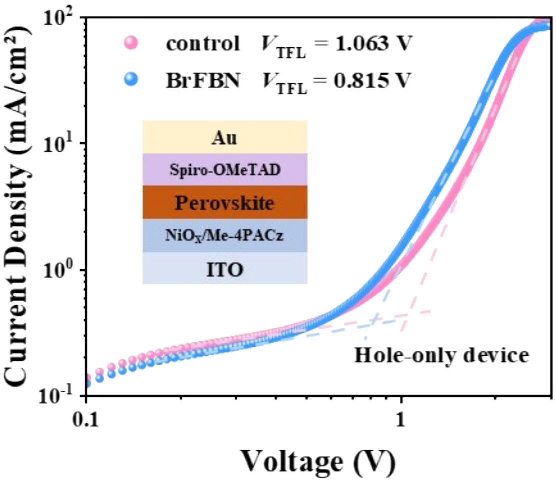

Figure S17. The dark *J*–*V* curves measured by the SCLC method for the device structure ITO/NiO_X/Me-4PACz/Perovskite/Spiro-OMeTAD/Au. The defect density is calculated using the SCLC results, and V_{TFL} is the trap filling voltage.

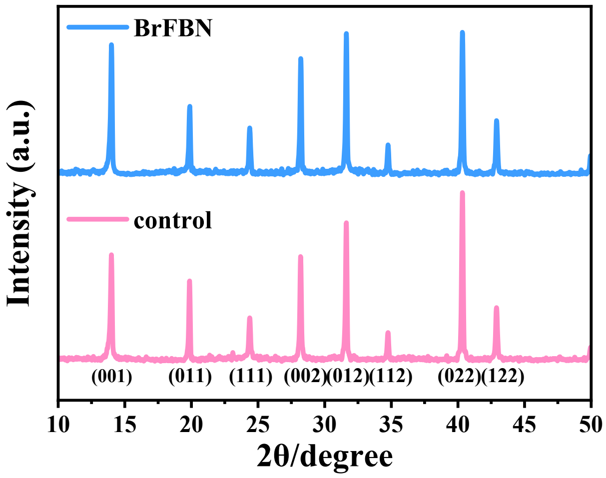

Figure S18. XRD patterns of control and BrFBN-modified perovskite films.

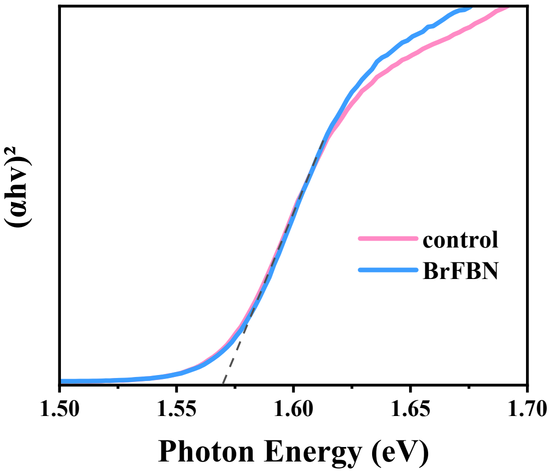

Figure S19. optical band gap of the control and BrFBN-modified perovskite films deposited on ITO substrate.

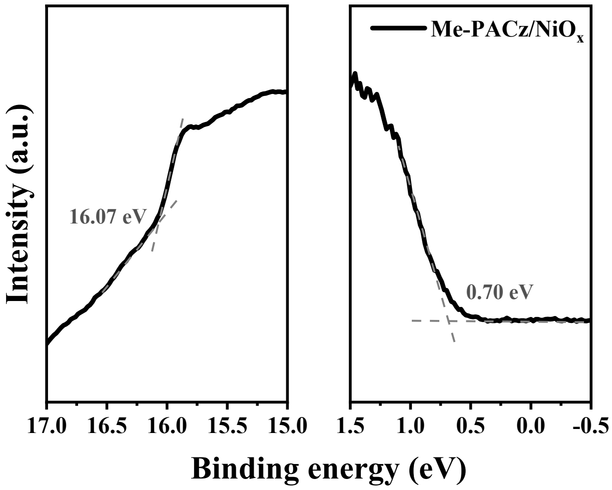

Figure S20. UPS data of the sample with ITO/NiO$_X$/Me-4PACz stacked.

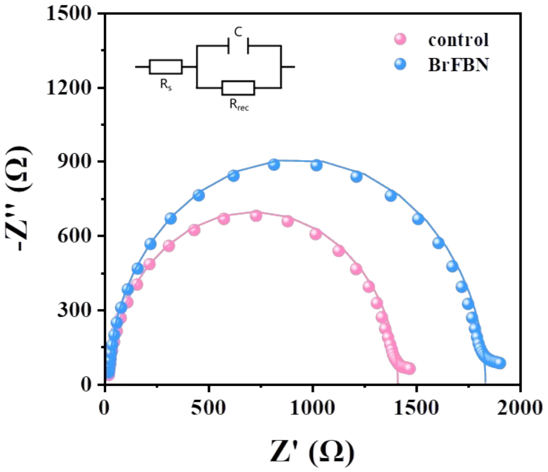

Figure S21. Electrochemical impedance spectra, the inset is the equivalent circuit, where R_s is the series resistance and R_{rec} is the charge recombination resistance.

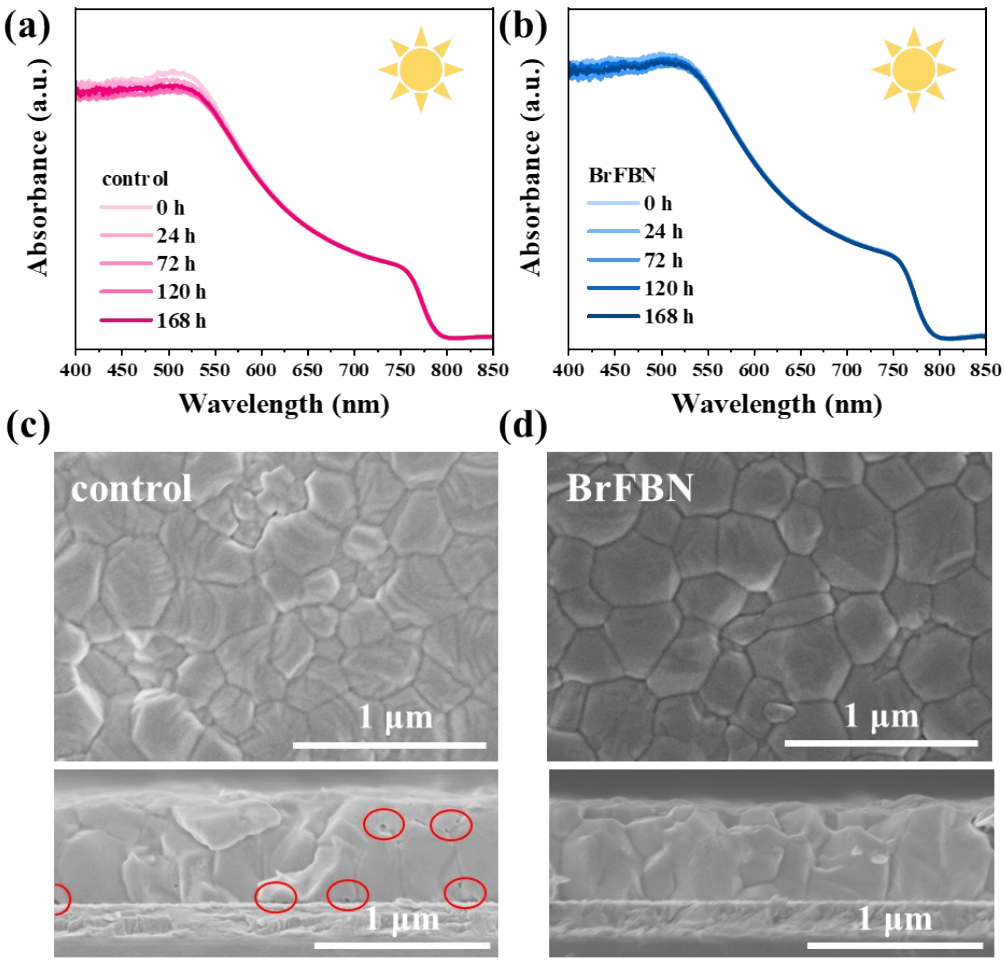

Figure S22. (a-b) The UV−vis absorption spectra of different treatment perovskite films under different aging times after photoaging at 100 mW/cm^2. (c-d) SEM images of different treatment perovskite films after photoaging at 100 mW/cm^2 for 168 h. Top row shows the top-view, and Bottom row shows the cross-view.

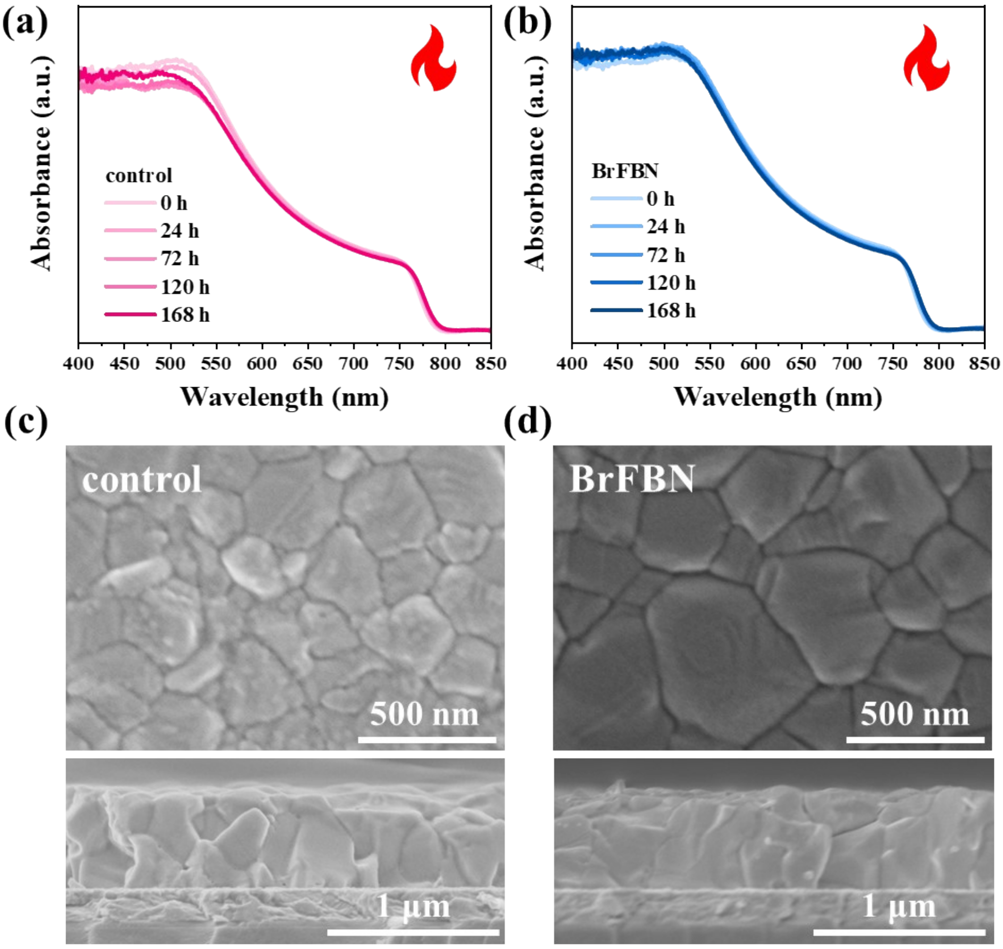

Figure S23. (a-b) The UV−vis absorption spectra of different treatment perovskite films under different aging times after thermal aging at 85 °C. (c-d) SEM images of different treatment perovskite films after thermal aging at 85 °C for 168 h. Top row shows the top-view, and Bottom row shows the cross-view.

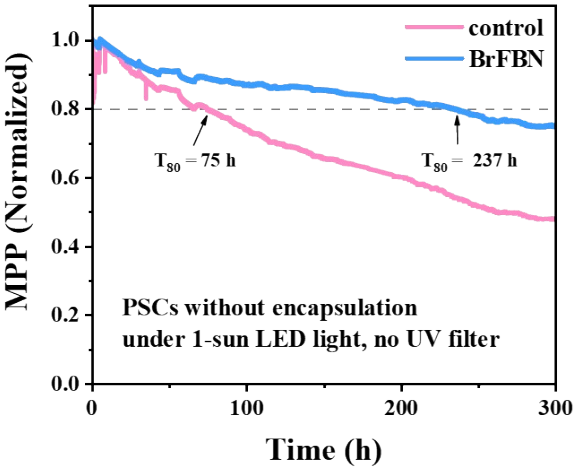

Figure S24. Operational stability of PSCs in the N_2-filled glove box at 100 mW/cm^2 from a white LED and MPP tracking.

Table S1. Performance summary for the devices with different BrFBA-modified. Statistics were calculated from 10 individual devices. (σ represents the standard deviation)

Samples		V_{OC} (V)	J_{SC} (mA/cm^2)	FF (%)	PCE (%)
control	Champion	1.152	24.81	81.94	23.42
	Mean±σ	1.147±0.004	24.21±0.31	80.04±1.42	22.24±0.64
2 mg/mL	Champion	1.157	24.96	81.37	23.50
	Mean±σ	1.157±0.003	24.53±0.54	79.63±1.61	22.61±0.88
3 mg/mL	Champion	1.154	25.04	82.04	23.70
	Mean±σ	1.152±0.006	24.56±0.61	81.00±0.57	22.92±0.61
4 mg/mL	Champion	1.153	24.78	81.08	23.16
	Mean±σ	1.150±0.004	24.59±0.36	79.80±0.80	22.57±0.47

Table S2. Performance summary for the devices with different BrFBP-modified. Statistics were calculated from 10 individual devices. (σ represents the standard deviation)

Samples		V_{OC} (V)	J_{SC} (mA/cm^2)	FF (%)	PCE (%)
control	Champion	1.152	24.81	81.94	23.42
	Mean±σ	1.147±0.004	24.21±0.31	80.04±1.42	22.24±0.64
2 mg/mL	Champion	1.153	24.99	81.43	23.46
	Mean±σ	1.151±0.005	24.59±0.40	80.44±1.27	22.77±0.47
3 mg/mL	Champion	1.156	25.02	83.24	24.08
	Mean±σ	1.157±0.007	24.55±0.59	81.51±1.00	23.16±0.77
4 mg/mL	Champion	1.160	24.89	81.69	23.59
	Mean±σ	1.161±0.001	24.38±0.48	80.17±1.21	22.69±0.51

Table S3. Performance summary for the devices with different BrFBN-modified. Statistics were calculated from 10 individual devices. (σ represents the standard deviation)

Samples		V_{OC} (V)	J_{SC} (mA/cm^2)	FF (%)	PCE (%)
control	Champion	1.152	24.81	81.94	23.42
	Mean±σ	1.147±0.004	24.21±0.31	80.04±1.42	22.24±0.64
2 mg/mL	Champion	1.151	24.96	82.78	23.78
	Mean±σ	1.149±0.006	24.58±0.43	80.94±1.77	22.86±0.82
3 mg/mL	Champion	1.159	25.27	83.36	24.42
	Mean±σ	1.158±0.004	24.73±0.42	82.23±0.90	23.56±0.55
4 mg/mL	Champion	1.156	24.99	82.96	23.96
	Mean±σ	1.153±0.006	24.54±0.37	81.27±1.52	23.00±0.53

Table S4. Energy of adsorption for a variety of DFT calculations including: the adsorption to the PbI2-rich surface of the perovskite via the -Br moiety or the the -R moiety (R=NH_2, OH, CN for BrFBA, BrFBP and BrFBN respectively) of the modifier, the adsorption to the FAI-rich surface of the perovskite, the gas phase adsorption energy to FAI and triiodide. Finally, we also calculated the dimerization energy in gas phase as well as in an intrinsic solvent reaction field (SCRF) using the parameters corresponding to water.

	E_{ads} (eV)							E_{dim} (eV)	
	Perovskite Surface 3x3x5			PbI_2 film 5x5x1	FA^+ (gas)	FAI (gas)	I_3^- (gas)	Dimer E	
	PbI_2-Rich		FAI-Rich	Optimal	X-FA^+	I-X-FA	X-I_3^-	Gas	SCRF =H_2O
	R-Ph-Br-Pb-	Br-Ph-R-Pb-							
BrFBA	-0.12	-0.43	-0.20	-1.19	-0.80	-0.56	-0.21	-0.39	-0.41
BrFBP	-0.32	-0.29	0.05	-0.95	-0.69	-0.36	-0.30	-0.24	-0.21
BrFBN	-0.13	-0.52	-0.04	-0.69	-1.04	-0.54	-0.47	-0.31	-0.17

Table S5. This is a companion table to Table S4 where we divided the gas phase dimerization of each passivant by the corresponding energy of adsorption. Wherever the ratio is >1 it can be said that dimerization may outcompete passivation and thus lower the availability of the passivant to interact with the perovskite surface. In cases where the adsorption energy is positive we write >>1 to indicate that dimerization greatly outcompetes it.

	E_{dim} : E_{ads} Ratio						
	Perovskite Surface 3x3x5			PbI_2 film 5x5x1	FA^+ (gas)	FAI (gas)	I_3^- (gas)
	PbI_2-Rich		FAI-Rich	Optimal	X-FA^+	I-X-FA	X-I_3^-
	R-Ph-Br-Pb-	Br-Ph-R-Pb-					
BrFBA	>>1	0.90	>>1	0.33	0.49	0.70	1.86
BrFBP	0.75	0.83	>>1	0.25	0.35	0.67	0.80
BrFBN	>>1	0.60	>>1	0.45	0.30	0.57	0.66

Table S6. Summary of the NMR spectral changes induced by mixing of BrFBN, DFBN, BrFBP, BrFBA with different perovskite precursor components (DMSO-d6, r.t.)

Molecule	Signal	pristine	+PbI_2	+ $PbBr_2$	+FAI	+CsI	+MABr
BrFBN	H_a	7.898	7.894	7.896	7.895	7.896	7.898
		7.913	7.910	7.911	7.911	7.911	7.913
	F	-104.453	-104.447	-104.445	-104.450	-104.451	-104.455
DFBN	H_a	7.447	7.447	7.447	7.447	7.448	7.449
	H_b	7.889	7.890	7.890	7.890	7.892	7.892
	F	-105.703	-105.702	-105.702	-105.706	-105.705	-105.709
BrFBP	H_a	7.360	7.357	7.358	7.357	7.357	7.358
		7.375	7.373	7.373	7.373	7.374	7.372
	F	-130.167	-130.162	-130.159	-130.168	-130.165	-130.159
BrFBA	H_a	7.188	7.185	7.186	7.186	7.186	7.186
		7.205	7.202	7.203	7.203	7.202	7.203
	H_b	5.410	5.406	5.409	5.407	5.407	5.409
	F	-129.401	-129.387	-129.392	-129.394	-129.394	-129.390

Signal	Pristine	+ BrFBN	+DFBN	+BrFBP	+BrFBA
FAI-1 (C-H)	7.854, s	7.855, bs	7.855, m	7.855, bs	7.854, s
FAI-2 (N-H)	8.827	8.66	8.64	8.658	8.821
FAI-3 (N-H)			8.67		
FAI-4 (N-H)		9.007	9.006	9.006	
FAI-5 (N-H)					
MABr-1 (N-H)	7.552, s	7.560 bs	7.563, bs	7.563, bs	7.561, s
MABr-2 (C-H)	2.368, s	2.370 bs	2.368, q	2.368, s	2.368, s

Table S7. Performance summary for the devices with different DFBN-modified. Statistics were calculated from 10 individual devices. (σ represents the standard deviation)

Samples		V_{OC} (V)	J_{SC} (mA/cm^2)	FF (%)	PCE (%)
control	Champion	1.150	24.87	81.81	23.39
	Mean±σ	1.145±0.005	24.24±0.59	79.91±1.16	22.18±0.80
1 mg/mL	Champion	1.154	24.86	82.14	23.56
	Mean±σ	1.147±0.005	24.42±0.62	80.48±0.92	22.55±0.73
2 mg/mL	Champion	1.162	24.94	82.61	23.94
	Mean±σ	1.155±0.04	24.64±0.26	81.94±0.81	23.32±0.42
3 mg/mL	Champion	1.158	24.90	82.49	23.79
	Mean±σ	1.153±0.006	24.56±0.64	81.01±1.18	22.93±0.75

Table S8. PL lifetimes of the control and BrFBN-modified films simulated by the double-exponential fitting of the PL decay curves.

Samples	A_1	τ_1 (ns)	A_2	τ_2 (ns)	τ_{ave} (ns)
control	0.25	7.27	0.95	843.77	841.87
BrFBN	0.15	7.33	1.60	1632.16	1631.48

Table S9. The fitted parameters of EIS curves.

Samples	R_s (Ω)	R_{rec} (Ω)
control	22.81	1392.00
BrFBN	21.87	1815.00

References

1. M. J. Frisch, G. W. Trucks, H. B. Schlegel, G. E. Scuseria, M. A. Robb, J. R. Cheeseman, G. Scalmani, V. Barone, G. A. Petersson, H. Nakatsuji, X. Li, M. Caricato, A. V. Marenich, J. Bloino, B. G. Janesko, R. Gomperts, B. Mennucci, H. P. Hratchian, J. V. Ortiz, A. F. Izmaylov, J. L. Sonnenberg, Williams, F. Ding, F. Lipparini, F. Egidi, J. Goings, B. Peng, A. Petrone, T. Henderson, D. Ranasinghe, V. G. Zakrzewski, J. Gao, N. Rega, G. Zheng, W. Liang, M. Hada, M. Ehara, K. Toyota, R. Fukuda, J. Hasegawa, M. Ishida, T. Nakajima, Y. Honda, O. Kitao, H. Nakai, T. Vreven, K. Throssell, J. A. Montgomery, J. E. Peralta, F. Ogliaro, M. J. Bearpark, J. J. Heyd, E. N. Brothers, K. N. Kudin, V. N. Staroverov, T. A. Keith, R. Kobayashi, J. Normand, K. Raghavachari, A. P. Rendell, J.C. Burant, S. S. Iyengar, J. Tomasi, M. Cossi, J. M. Millam, M. Klene, C. Adamo, R. Cammi, J. W. Ochterski, R. L. Martin, K. Morokuma, O. Farkas, J. B. Foresman, D. J. Fox, Gaussian 16 Revision C.01, 2016, Gaussian 16, Revision C.01, Gaussian, Inc., Wallin.
2. J. Tomasi, B. Mennucci, R. Cammi, *Chem. Rev.*, 2005, **105**, 2999.
3. G. Kresse, J. Hafner, *Phys. Rev. B* ,1994, **49**, 14251.
4. J. P. Perdew, K. Burke, M. Ernzerhof, *Phys. Rev. Lett.*, 1996, **77**, 3865.
5. S. Grimme, J. Antony, S. Ehrlich, H. Krieg, *J. Chem. Phys.*, 2010, **132**, 154104.
6. P. E. Blöchl, *Phys. Rev. B* 1994, **50**, 17953.
7. G. Kresse, D. Joubert, *Phys. Rev. B*, 1999, **59**, 1758.

8. I. Płowaś-Korus, J. Kaczkowski, *New J. Chem.* 2022, **46**, 15381.
9. S. Cao, L. G. Gutsev, Z. Bi, Y. Zheng, X. Xu, Y. Zhu, L. Zhong, J. Zheng, G. Xu, P. A. Troshin, S. (Frank) Liu, K. Wang, G. Cedric, G. Antonio, Z. Ren, L. Gang, *Chem. Eng. J.*,2023, **474**, 145707.
10. B. Liu, Y. Wang, Y. Wu, Y. Zhang, J. Lyu, Z. Liu, S. Bian, X. Bai, L. Xu, D. Zhou, B. Dong, H. Song, *Adv. Energy Mater.*, 2023, **13**.
11. Y. Wu, Q. Wang, Y. Chen, W. Qiu, Q. Peng, *Energy Environ. Sci*. 2022, **15**, 4700.